COMPARISON OF REYNOLDS STRESS TRANSPORT AND EDDY-VISCOSITY
TURBULENCE CLOSURE PREDICTIONS FOR A MACH 6 SHOCK
WAVE-BOUNDARY-LAYER INTERACTION ON A FLARED-CONE GEOMETRY

By

NOAH ZAMBRANO

A THESIS PRESENTED TO THE HERBERT WERTHEIM COLLEGE OF ENGINEERING
OF THE UNIVERSITY OF FLORIDA IN PARTIAL FULFILLMENT
OF THE REQUIREMENTS FOR THE DEGREE OF
BACHELOR OF SCIENCE IN AEROSPACE ENGINEERING

UNIVERSITY OF FLORIDA

2022

TABLE OF CONTENTS

LIST OF TABLES

LIST OF FIGURES

LIST OF ABBREVIATIONS

A	Reynolds stress flatness parameter
A_2, A_3	Reynolds stress anisotropy invariants
$\tilde{a}_{ij}$	Reynolds stress anisotropy tensor component
c	Speed of sound
D	Reynolds stress diffusion coefficient
$D^{\tilde{k}}$	Diffusion rate of kinetic turbulence energy, m^2/s^3
D_{ij}	Specific diffusion tensor component, m^2/s^3
D_{ij}^p	Specific pressure diffusion tensor component, m^2/s^3
D_{ij}^v	Specific viscous diffusion tensor component, m^2/s^3
E	Specific total energy, m^2/s^3
G_{ij}	Buoyancy production, m^2/s^3
H	Specific total enthalpy, m^2/s^3
h	Specific enthalpy, m^2/s^3
k_t	Thermal conductivity, W/mK
$\tilde{k}$	Specific kinetic turbulence energy, m^2/s^2
M_{ij}	Specific tensor of fluctuating mass flux contribution component, m^2/s^3
M	Mach number
$\overline{M}$	Molecular mass
n_i	Wall-normal vector component
P	Pressure, Pa
P_{ij}	Specific production tensor component, m^2/s^3
q_i	Heat flux component, W/m^2
$q_i^{(t)}$	Turbulent heat flux component, W/m^2
R_{univ}	Universal gas constant, m^2/s^2
$\tilde{R}_{ik}$	Reynold stress components, m^2/s^3
S	Sutherland's constant
t	Time, s
T	Temperature, K
T_{ij}	Specific turbulent transport tensor component, m^2/s^3
U_i	Velocity component, m/s
u_i''	Fluctuating velocity component, m/s
x_i	Cartesian coordinates, m
Z	Compressiblity factor
α	Blending parameter
δ_{ij}	Kronecker delta function
ε	Dissipation rate, m^2/s^3
ε_{ij}	Component of dissipation rate tensor, m^2/s^3
γ_m	Dilatation dissipation, m^2/s^3
μ	Dynamic viscosity, kg/m s
μ_t	Turbulent eddy viscosity, $text m^2/s$
ν	Kinematic viscosity, m^2/s
Π_{ij}	Specific pressure-strain correlation tensor component, m^2/s^3
ρ	Density kg/m^3
τ_{ik}	Viscous stress component, N/m^2

Abstract of Thesis Presented to the Herbert Wertheim Collge of Engineering
of the University of Florida in Partial Fulfillment of the
Requirements for the Degree of Bachelor of Science in Aerospace Engineering

COMPARISON OF REYNOLDS STRESS TRANSPORT AND EDDY-VISCOSITY
TURBULENCE CLOSURE PREDICTIONS FOR A MACH 6 SHOCK
WAVE-BOUNDARY-LAYER INTERACTION ON A FLARED-CONE GEOMETRY

By

Noah Zambrano

May 2022

Chair: Steven Miller
Major: Aerospace Engineering

An examination of a Mach 6 turbulent shock wave-boundary-layer interaction on a canonical flared-cone geometry is undertaken. The flow structure, surface pressure, and heat flux along the flared cone is predicted using the Reynolds-Averaged Navier-Stokes equations, and results are compared to experimental data and previous simulations of the same experiment. Two Reynolds Stress Transport turbulence closures (linear-pressure strain and elliptic blending) and an eddy-viscosity closure (Menter k-ω Shear Stress Transport) are used to close the equations. Model predictions are compared to experimental results to quantify their error. The eddy-viscosity model is found to outperform the Reynolds Stress Transport closures both qualitatively and quantitatively for this specific case. The Reynolds Stress Transport models over predict separation forward of the expected location by at least 6 cm and at most by 14 cm, while the eddy-viscosity model separation point is accurate when qualitatively compared to experimental results. Excessive peak heat flux and surface pressure values were found with all model predictions ranging from 37%-200% error for heat flux and 30%-50% for surface pressure. Analysis of the results show that the Reynolds Stress Transport models did not predict the turbulent dissipation rate accurately enough due to the use of a k-ε model for the turbulent dissipation rate. Shortcomings for closures in the Favré-averaged Navier-Stokes equations are discussed and a potential solution to improve heat flux predictions is recommended.

CHAPTER 1
INTRODUCTION

1.1 Overview

Computational fluid dynamics (CFD) is widely used in the aerospace industry to predict flow-fields and aid in engineering design. This is especially true for flow regimes where experiments are unfeasible or difficult to conduct, such as hypersonic flow-fields. To obtain a reasonable prediction of the flow-field, the CFD models must be physically representative of the true conditions. In the past decade, it has been shown that many engineering quantities, such as surface pressure or heat flux, are not accurately predicted using the current Reynolds-averaged Navier-Stokes (RANS) CFD models[1] This work will explore the over-prediction of heat transfer by contemporary RANS closures for high-speed flows, particularly a Mach 6 flow with a turbulent shock-wave boundary-layer interaction (SBLI) on a flared-cone geometry. SBLI introduce difficulties in modeling due to the intense adverse pressure gradient on the boundary-layer which causes it to thicken or separate[2].

Turbulence is an irregular condition with random fluctuations of the flow quantities in space and time. To achieve ideal predictions, the turbulent motion should be resolved in space-time, to avoid any modeling errors. This is achieved by direct numerical simulation (DNS) but is impractical in time-constrained projects due to the small grid scales required to resolve all turbulent motion[1], especially for high Reynolds number flows. A reduced computational demand may be achieved by explicitly resolving the largest scales of turbulence in large eddy simulations (LES). In LES, the smallest scales of turbulence must be modeled with a subgrid-scale model, where assumptions at those scales keep the modeling error small. However, at large Reynolds numbers, even the largest turbulence scale become very small and represents a computational burden for full-model simulations[3].

A more computationally inexpensive method is the traditional way of modeling turbulence and solving the RANS equations. In RANS CFD, only the mean flow is considered and turbulence enters the equations through an additional term called the Reynolds stress[1]. The turbulence model is used to provide a closure to the RANS equations by solving for the Reynolds stresses. Turbulence closures that solve directly for these Reynolds stresses are called Reynolds

Stress Transport (RST) models or second-moment closures[4]. This paper focuses on RST models, specifically the linear pressure-strain closure by Launder and Shima[5] and the elliptic blending closure by Lardeau and Manceau[6]. In addition, an eddy-viscosity model is used to compare against the RST model predictions. Eddy-viscosity models rely on the Boussinesq hypothesis where it is assumed that turbulent motion is modeled as a state of flow where there is an effective higher viscosity, called the eddy viscosity[1]. Through this hypothesis, only one parameter needs to be determined and this approach greatly simplifies turbulence modeling schemes. RANS eddy-viscosity models remain the most popular closures for CFD due to its quick convergence and ability to perform steady simulations. The shear stress transport (SST) k-ω eddy-viscosity model by Menter[9] is used due to its ability to predict flow separation and its wide-spread use in industry.

1.2   Case Study and Methodologies

This research aims to quantify the error in heat flux and surface pressure prediction for eddy-viscosity and RST models by comparing predictions with measurement data. The selected case is the flared-cone geometry with experimental data at Mach 6 by Holden et al.[7]. See Fig. 1-1 for the general shape of the flared-cone. The shock wave-boundary-layer interaction of interest occurs at the flare-cone intersection portion of the geometry. Due to the sharp changes in geometry, a λ-shock interaction is generated with a separation shock intersecting a reattachment shock. Due to the λ-shock interaction, a slip-line is expected to appear in the solution along the flare. Additionally, a large singular separation bubble is expected to form on the cone and flare. See Fig. 1-2 for the SBLI structure of interest and the labels of the main features.
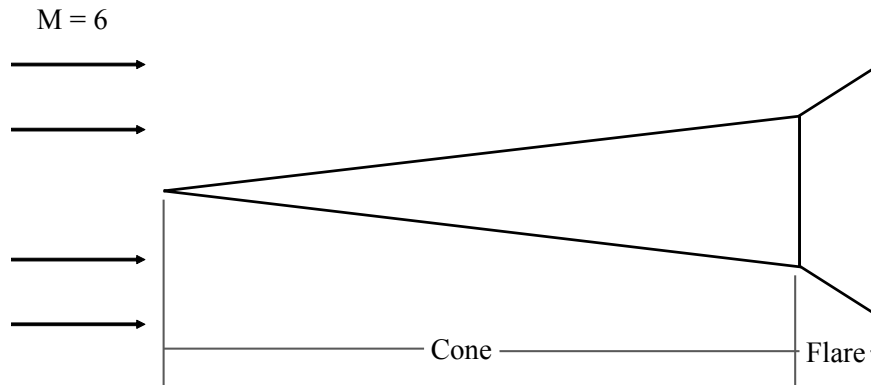
Figure 1-1. Flared cone of Holden et al.[7].
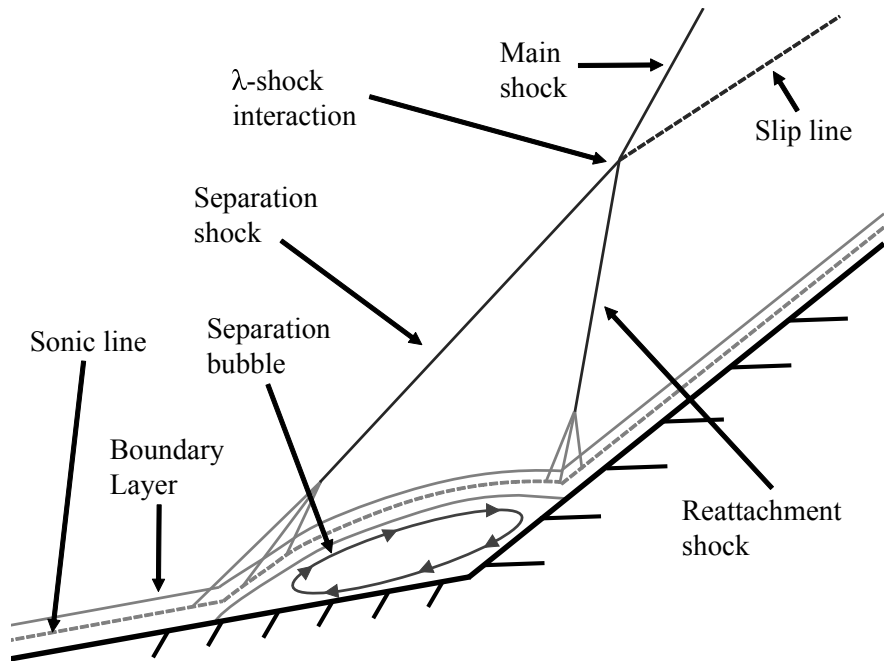
Figure 1-2. SBLI structure and dominant features.

The computation is completed using a commercial CFD solver, STAR-CCM+ by Siemens. The discretization methods and important scheme selection is presented in the paper. Additionally, a grid convergence study is completed alongside adaptive meshing. The normalized pressure gradient algorithm by Cross and West[8] for the adaptive mesh is explained with recommended parameters for successful shock-capturing meshing. The grid convergence study

examines the initial grid based on conditions far from the SBLI, with the goal to establish initial grid convergence suitable to perform adaptive refinement on. The numerical methods and grid are checked with data of Cross and West[6], where the authors used the same eddy-viscosity model, numerics, boundary conditions, and adaptive meshing technique for a CFD simulation of the same flared-cone geometry.

1.3 Outcomes

It is hypothesized that RST closures should have the potential to out-perform the eddy-viscosity models because they do not rely on the Boussinesq hypothesis. However, since eddy-viscosity models are popular in industry, the coefficients tend to be calibrated to a wide range of flow-regimes. In addition, the RST models used in this work rely on the k-ε formulation and thus are not expected to perform as well as the k-ω SST model in adverse pressure gradients[1]. This is important as the model performance in adverse pressure gradients impacts the separation location. Accurate modeling of the separation and reattachment is important because the downstream features depend on the location and length of the separation bubble. The re-attachment point is where the peak heat flux occurs. To properly compare heat flux predictions to experimental measurements, the reattachment point must be close to that observed in the experiment. By quantifying the error in heat flux and surface pressure when compared to experimental data, this study will aid in finding which of the three selected closures are more applicable to high-speed SBLI.

CHAPTER 2
GOVERNING EQUATIONS

2.1   Favré-Averaged Navier-Stokes Equations

The Favré-averaged Navier-Stokes (FANS) equations are used to solve for the fluid
flow-field. Simple averages $\overline{\phi}$ are indicated by an overbar while mass weight averages $\tilde{\phi} = \rho/\overline{\phi}\rho$
are indicated by a tilde. Einstein notation is used. The Favré-averaged Navier-Stokes and energy
equations are

$$\frac{\partial \overline{\rho}}{\partial t} + \frac{\partial}{\partial x_k}\left(\overline{\rho}\tilde{U}_k\right) = 0, \tag{2-1}$$

$$\frac{\partial \left(\overline{\rho}\tilde{U}_i\right)}{\partial t} + \frac{\partial}{\partial x_k}\left(\overline{\rho}\tilde{U}_i\tilde{U}_k\right) + \frac{\partial}{\partial x_k}\left(\overline{\rho}\tilde{R}_{ik}\right) = -\frac{\partial \overline{p}}{\partial x_i} + \frac{\partial \overline{\tau}_{ik}}{\partial x_k}, \tag{2-2}$$

and,

$$\frac{\partial \left(\overline{\rho}\tilde{E}\right)}{\partial t} + \frac{\partial}{\partial x_k}\left(\overline{\rho}\tilde{H}\tilde{U}_k\right) + \frac{\partial}{\partial x_k}\left(\overline{\rho}\tilde{R}_{ik}\tilde{U}_i\right) = \frac{\partial \overline{\tau}_{ik}\tilde{U}_i}{\partial x_k} + \overline{\rho}D^{\tilde{k}} - \frac{\partial \overline{q}_k}{\partial x_x} - \frac{\partial \overline{q}_k^t}{\partial x_x}. \tag{2-3}$$

The equations are further simplified by using the axisymmetric formulation of the continuity,
momentum, energy, and density equations. A real gas model (equilibrium air) is used with the
assumption that the time scale of molecular dissociation, internal energy excitation, and
ionization effects are much shorter than the time scale of the flow. In this case, the properties of
the flow, such as the density, specific heat, and transport properties, become expressions of two
thermodynamic variables. These expressions take the form of curve fits from the work of
Gupta[10]. This model provides the compressibility factor as a field function from which density
can be found as

$$Z(T,P) = \frac{M_0}{\overline{M}} = \frac{\rho_0}{\rho}. \tag{2-4}$$

With the equilibrium air real gas model, gas material properties (viscosity, thermal conductivity,
specific heat, and speed of sound) are automatically computed as functions of temperature and
pressure. Thermal conductivity and dynamic viscosity utilize Sutherland's laws,

$$\frac{\mu}{\mu_0} = \left(\frac{T}{T_0}\right)^{3/2}\left(\frac{T_0+S}{T+S}\right) \tag{2-5}$$

and

$$\frac{k}{k_0} = \left(\frac{T}{T_0}\right)^{3/2}\left(\frac{T_0+S}{T+S}\right), \tag{2-6}$$

where the Sutherland constant used is $S = 111$ K for air. Energy and enthalpy are found as

$$E = H - \frac{p}{\rho} \tag{2-7}$$

and

$$H = h + \frac{|\mathbf{v}|^2}{2}. \tag{2-8}$$

Closure equations and terms are required for the RANS equations. Reynolds-averaging introduces a Reynolds stress term,

$$\rho \tilde{U}_k = \overline{\rho u_i'' u_k''}, \tag{2-9}$$

in the momentum equation with components that describe the velocity fluctuations. Reynolds-averaging the energy equation also introduces the turbulent heat flux vector,

$$\overline{q}_k^t = \overline{\rho h'' u_k''}, \tag{2-10}$$

that represents the relationship between velocity and temperature fluctuations, and the diffusion of specific turbulent kinetic energy term,

$$\overline{\rho} D^{\tilde{k}} = \frac{\partial}{\partial x_k} \left(-\frac{1}{2} \overline{\rho u_i'' u_i'' u_k''} + \overline{\tau_{ik} u_i''} \right). \tag{2-11}$$

A Reynolds stress transport equation is derived from the momentum equation

$$\frac{\partial (\overline{\rho} \tilde{R}_{ij})}{\partial t} + \frac{\partial}{\partial x_k} (\overline{\rho} \tilde{R}_{ij} \tilde{U}_k) = \overline{\rho} P_{ij} + \overline{\rho} \Pi_{ij} - \overline{\rho} \varepsilon_{ij} + \overline{\rho} D_{ij} + \overline{\rho} M_{ij}, \tag{2-12}$$

where five new terms need to be solved for to close the RANS equations. The terms are the production term,

$$\overline{\rho} P_{ij} = -\overline{\rho}_{ik} \frac{\partial_j}{\partial x_k} - \overline{\rho} \tilde{R}_{jk} \frac{\partial_i}{\partial x_k} \tag{2-13}$$

the pressure-strain correlation,

$$\overline{\rho} \Pi_{ij} = \overline{p' \left(\frac{\partial u_i''}{\partial x_j} + \frac{\partial u_j''}{\partial x_i} \right)} \tag{2-14}$$

13

the dissipation term,

$$\overline{\rho}\varepsilon_{ij} = \overline{\tau'_{ik}\frac{\partial u''_i}{\partial x_j}} + \overline{\tau'_{jk}\frac{\partial u''_j}{\partial x_k}} \tag{2-15}$$

the diffusion term,

$$\overline{\rho}D_{ij} = -\frac{\partial}{\partial x_k}\left[\overline{\rho u''_i u''_j u''_k}\right] + \frac{\partial}{\partial x_k}\left[\overline{\rho \tau'_{ik} u''_j} + \overline{\rho \tau'_{jk} u''_i}\right] - \frac{\partial}{\partial x_k}\left[\overline{\rho p' u''_i}\delta_{jk} + \overline{\rho p' u''_j}\delta_{ik}\right] \tag{2-16}$$

and finally the compressibility effects term,

$$\overline{\rho}M_{ij} = \frac{1}{2}\left(\overline{\rho}T_{ii} + \overline{\rho}D^v_{ii}\right). \tag{2-17}$$

The diffusion term is modeled with an isotropic form of the turbulent diffusion term adopted from Lien[11]

$$\overline{\rho}D_{ij} = \frac{\partial}{\partial x_k}\left(\mu + \frac{\mu_t}{\sigma_k}\right)\frac{\partial \tilde{R}_{ij}}{\partial x_l}, \tag{2-18}$$

where the turbulent viscosity μ_t is computed

$$\mu_t = \rho C_\mu \frac{k^2}{\varepsilon} \tag{2-19}$$

with the model coefficient C_μ and the turbulent kinetic energy k.

The dissipation term is modeled with an isotropic turbulent dissipation term and the dilatation dissipation rate as

$$\overline{\rho}\varepsilon_{ij} = \frac{2}{3}\overline{\rho}\varepsilon + \frac{2}{3}\gamma_m. \tag{2-20}$$

The dilatation dissipation is modeled in the same way as in the k-ε model by Sarkar et al.[12],

$$\gamma_m = \frac{\rho C_m k \varepsilon}{c^2}. \tag{2-21}$$

The turbulent dissipation rate is also modeled by solving a transport equation analogous to the k-ε model using the production tensors

$$\frac{\partial}{\partial t}(\rho\varepsilon) + \frac{\partial}{\partial x_k}(\rho\varepsilon\overline{v}) = \frac{\partial}{\partial x_k}\left[\left(\overline{\mu} + \frac{\mu_t}{\sigma_\varepsilon}\right)\frac{\partial \varepsilon}{\partial x_k}\right] + \frac{\varepsilon}{k}\left[C_{\varepsilon 1}\left(\frac{\overline{\rho}P_{kk}}{2} - \frac{C_{\varepsilon 3}\overline{\rho}G_{kk}}{2}\right) - C_{\varepsilon 2}\rho\varepsilon\right]. \tag{2-22}$$

The pressure-strain term, the most difficult to model, is found using two different models: the

linear pressure-strain two-layer model and the elliptic blending model.

2.2   Linear Pressure-Strain Two-Layer Model

The linear pressure-strain model assumes that the mean and turbulent strains influence the pressure fluctuations[5]. Additionally, the rigid walls create "echo" effects that further influence pressure fluctuations[13]. The pressure-strain term takes the form of the summation of four terms,

$$\Pi_{ij} = \Pi_{ij,1} + \Pi_{ij,2} + \Pi_{ij,1}^w + \Pi_{ij,2}^w, \tag{2-23}$$

where each term is defined as

$$\Pi_{ij,1} = -c_1 \varepsilon a_{ij}, \tag{2-24}$$

$$\Pi_{ij,2} = -c_2 \left(P_{ij} - \frac{2}{3} \delta_{ij} P_{kk} \right), \tag{2-25}$$

$$\Pi_{ij,1}^w = c_1^w \left(\frac{\varepsilon}{k} \right) \left[\overline{u_k u_m} n_k n_m \delta_{ij} - \frac{3}{2} \overline{u_k u_i} n_k n_i - \frac{3}{2} \overline{u_k u_j} n_k n_j \right] f, \tag{2-26}$$

$$\Pi_{ij,2}^w = c_2^w \left[\Pi_{km2} n_k n_m \delta_{ij} - \frac{3}{2} \Pi_{ik2} n_k n_i - \frac{3}{2} \Pi_{jk2} n_k n_j \right] f, \tag{2-27}$$

and,

$$f = 0.4 \frac{k^{3/2}}{\varepsilon x}. \tag{2-28}$$

The two-layer formulation modifies the coefficients[5] as

$$c_1 = 1 + 2.58 A A_2^{1/4} (1 - \exp(-0.0067 Re_t^2)), \tag{2-29}$$

$$c_2 = 0.75 \sqrt{A}, \tag{2-30}$$

$$c_1^w = \frac{-2}{3} c_1 + 1.67, \tag{2-31}$$

and,

$$c_2^w = \max[(\frac{2}{3}c_2 - \frac{1}{6})/c_2, 0].$$ (2-32)

2.3 Elliptic Blending Model

The elliptic blending model utilized is that of Lardeau and Manceau[6]. This is a low-Reynolds number model based on an inhomogeneous near-wall formulation of the quasi-linear quadratic pressure-strain term. A blending function is used to blend the viscous sub-layer with the log-layer formulation for the pressure-strain term and dissipation term,

$$\Pi_{ij} - \varepsilon_{ij} = (1 - \alpha^3)(\Pi_{ij}^w - \varepsilon_{ij}^w) + \alpha^3(\Pi_{ij}^h - \varepsilon_{ij}^h).$$ (2-33)

The solution to the elliptic equation is the blending parameter,

$$\alpha - L^2 \nabla^2 \alpha = 1.$$ (2-34)

The length scale is defined as

$$L = C_l \max\left(\frac{k^{3/2}}{\varepsilon}, C_\eta \frac{v^{3/4}}{\varepsilon^{1/4}}\right).$$ (2-35)

The quasi-linear Speziale-Sarkar-Gatski (SSG) model by Speziale et al.[14] is used to model the pressure-strain term in the outer-region,

$$\Pi_{ij}^h = -\left(C_1 + C_2^* \frac{P}{\varepsilon}\right)\varepsilon a_{ij} + (C_3 - C_3^* \sqrt{a_{kl}a_{kl}})kS_{ij}$$
$$+ C_4 k \left(a_{ik}S_{jk} + a_{jk}S_{ik} - \frac{2}{3}a_{lm}S_{lm}\delta_{ij}\right) + C_5 k(a_{ik}W_{jk} + a_{jk}W_{ik}).$$ (2-36)

The near wall pressure strain is modeled as,

$$\Pi_{ij}^w = -5\frac{\varepsilon}{k}\left[\overline{u_i u_k}n_j n_k + \overline{u_j u_k}n_i n_k - \frac{1}{2}\overline{u_k u_l}n_k n_l(n_i n_j \delta_{ij})\right],$$ (2-37)

using the vector normal from the wall which is found with the elliptic blending parameter,

$$n_k = \frac{\partial \alpha / \partial x_k}{\sqrt{\frac{\partial \alpha}{\partial x_l}\frac{\partial \alpha}{\partial x_l}}}.$$ (2-38)

16

Similarly, the dissipation rate tensor is modeled separately for the outer and near-wall region as

$$\varepsilon_{ij}^w = \frac{\overline{u_i u_j}}{k}\varepsilon \tag{2-39}$$

and

$$\varepsilon_{ij}^h = \frac{2}{3}\varepsilon\delta_{ij}. \tag{2-40}$$

For the elliptic blending model, the eddy viscosity μ_t is redefined as

$$\mu_t = \rho C_\mu k T, \tag{2-41}$$

based on the turbulent time-scale T,

$$T = \max\left(\frac{k}{\varepsilon}, C_t\sqrt{\frac{\nu}{\varepsilon}}\right). \tag{2-42}$$

An additional term is added to the model of the dissipation rate term to improve performance in the near-wall region,

$$E = A_1 \nu \overline{u_k u_l} n_k n_l \frac{k}{\varepsilon}(1-\alpha^3)\left(\frac{\partial \|S_{ij}n_i\| n_k}{\partial x_k}\right)^2. \tag{2-43}$$

CHAPTER 3
NUMERICAL METHODS

The commercial CFD code, STAR CCM+ by Siemens, is used as the numerical solver for the governing equations outlined in Chapter 2. STAR CCM+ is a finite-volume solver that discretizes the governing equations in space and time and then solves the resulting linear equations with an algebraic multigrid solver. Steady-state simulations are performed. The conservation equations are written in the form of a general transport equation, which is then integrated over a control volume. Applying Gauss's Theorem yields a form of an integral transport equation that is easily discretizable,

$$\frac{d}{dt}\int_V \rho\phi dV + \int_A \rho\mathbf{v}\phi \cdot \mathbf{a} = \int_A \Gamma\nabla\phi\mathbf{a} + \int_V S_\phi dV. \tag{3-1}$$

Surface integrals are evaluated using quadrature approximations and expressed in terms of variables on the cell face. A second-order midpoint rule is employed,

$$\int_A \mathbf{J}^\phi \cdot d\mathbf{a} \approx \sum_f \mathbf{J}_f^\phi \cdot \mathbf{a}_f. \tag{3-2}$$

The volume integrals are approximated by the product of the mean value of the source term at the cell center and the volume of the cell. To make this approximation second-order accurate, the cell face center is the weight area center and the cell center is the volume center,

$$\int_V S_\phi dV \approx S_{\phi_0} V_0 \tag{3-3}$$

and

$$\frac{d}{dt}(\rho\phi V_0) + \sum_f [\rho\phi(\mathbf{v}\cdot\mathbf{a})]_f = \sum_f (\Gamma\nabla\phi\cdot\mathbf{a})_f + (S_\phi V)_0. \tag{3-4}$$

The convective flux term in the discretized volume integral can be rearranged in terms of the mass flow rate and fluid property at the cell face,

$$\rho\phi(\mathbf{v}\cdot\mathbf{a})_f = \dot{m}_f \phi_f. \tag{3-5}$$

It is noted that the scheme selected for finding the fluid property at the face has a large impact on numerical stability. The convective flux scheme used is the hybrid monotonic upstream-centered scheme for conservation laws (MUSCL) 3rd-order/central-differencing scheme where a

first-order upwind differencing scheme is used in regions of non-smooth flows (shocks),

$$(\dot{m}_f \phi) = \begin{cases} \dot{m}\phi_{\text{FOU}} & \xi < 0 \text{ or } \xi > 1 \\ \dot{m}(\sigma_{\text{MUSCL}}\phi_{\text{MUSCL}} + (1 - \sigma_{\text{MUSCL}})\phi_{CD3}) & 0 < \xi < 1. \end{cases} \tag{3-6}$$

In addition, the inviscid fluxes are evaluated using the ASUM+ flux-vector splitting scheme. The use of the AUSM+ scheme is required for numerical stability. The inviscid fluxes are

$$f = f^c + P = 0.5(m_i + |m_i|)(\phi)_0^T + 0.5(m_i - |m_i|)(\phi)_1^T + P_i. \tag{3-7}$$

The mass flux and pressure flux are calculated based on local flow characteristics for correct information propagation inside the fluid for convective and acoustic processes.

3.1   Boundary Conditions

Boundary conditions were selected based on free-stream values from run 33 of Holden et al.[7]. Boundary conditions at the walls are set with the no-slip condition and are isothermal. The outlet was set as a pressure outlet with static pressure and temperature specified, and the inflow and far-field were set as free-stream boundary conditions with direction specified. Boundary conditions are tabulated in Table 3-1. Fig. 3-1 specifies the dimensions of the domain in centimeters along with labels for each boundary.

Table 3-1. Boundary Conditions.

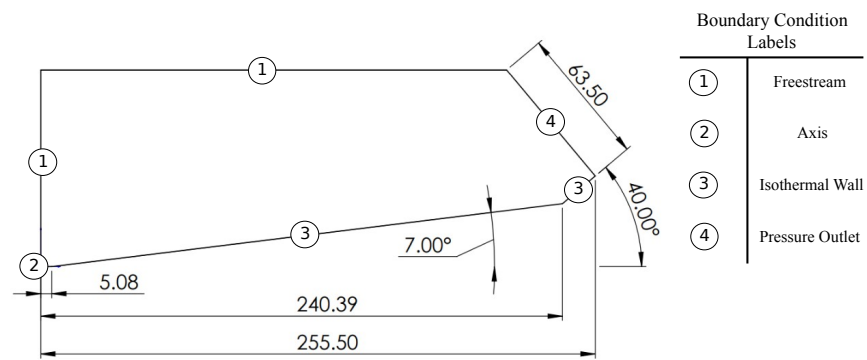| Quantity	Freestream	Wall	Outlet
M	6.17	0	Not Fixed
u (m/s)	931.25	0	Not Fixed
v (m/s)	0	0	Not Fixed
w (m/s)	0	0	Not Fixed
T (K)	56.4	298	56.4
P (Pa)	1418	Not Fixed	1418

Figure 3-1. Flared cone geometry domain dimensions (cm).

CHAPTER 4
SPATIAL DISCRETIZATION AND ADAPTATION

4.1   Initial Mesh

A triangular grid was used for the freestream spatial discretization with a prism layer used for the boundary layer. Turbulence models require that the full boundary layer be resolved, thus the distance from the wall to the first grid point must be approximately equal to one. A prism layer height of 0.012 meters was used on the cone while a height of 0.005 meters was used on the flare. This prism layer height was confirmed to capture the boundary layer height at which velocity reached 99% local freestream velocity by examining the profile in inner coordinates.

4.2   Adaptive Mesh

To reduce the manual work of placing refinement sections for shocks in the grid, a semi-automated process was developed using a grid adaptation technique known as normalized pressure gradient refinement[8]. This method of refinement calculates regions of high-pressure gradients and marks the cells for refinement, which are then re-sized and stored as a table in STAR CCM+. Fig. 4-1 is an example of the marking of the cells, where the blue is for coarsening, yellow stays the same size, and brown cells are refined.

With a new set of cell sizes specified, the mesh is re-generated with the table-based refinement enabled and the process is repeated until sufficient shock refinement is attained. The pressure gradient is normalized by the absolute pressure and scaled by the cell length. Cell length was used as the scaling factor because it was found to be a more appropriate characterization of the cell size as opposed to cell area. Cell length is the longest dimension of the cell and thus further scaled the pressure gradient for highly anisotropic cells, like prism layers. The method for calculating cell length for axisymmetric simulations was taken from Cross and West[8]. In addition, a condition was added to stop refinement near the wall and avoid excessive refinement of the prism layer. Cells were refined or coarsened by a factor of two after their selection. Fig. 4-2 shows the flow of information and various constraints in the normalized pressure gradient adaptive method, where P is the pressure, CL is the cell length, RT and CT are the refinement and coarsening threshold for the pressure gradient, CR is the cell refinement flag, and CS is the cell size. Maximum and minimum cell size thresholds are indicated by the subscripts min and max for
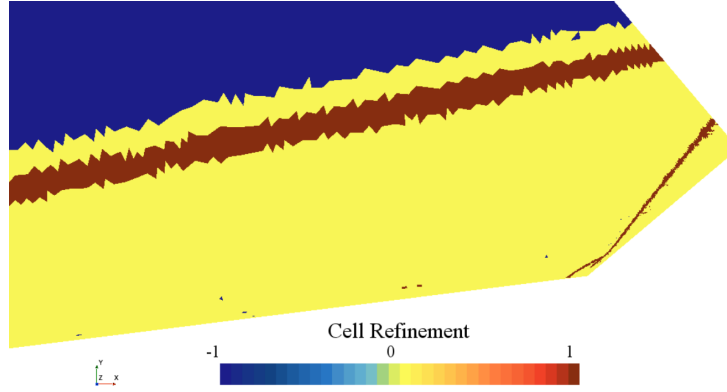
the *CS* variable.

Figure 4-1. Close-up of the refinement field for adaptive meshing near the flared portion of the geometry.
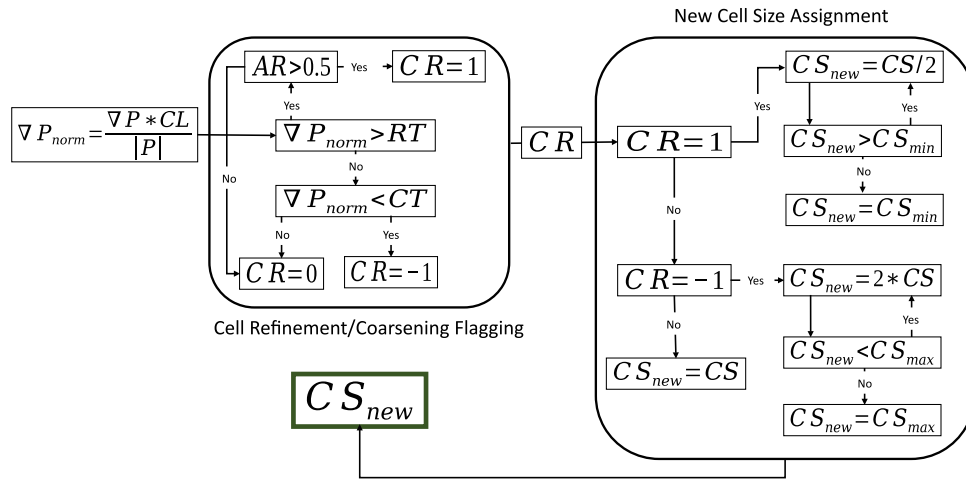

Figure 4-2. Algorithm flow chart for adaptive meshing technique.

CHAPTER 5
RESULTS

5.1 Overview

Grid convergence and adaptive meshing results are discussed below along with notes on the meshing method. The results from the Menter k-ω SST, RST elliptic blending, and linear pressure-strain two-layer closures are also discussed and compared to each other. Simulation results are compared to experimental results of Holden et al.[7] and errors are quantified. In addition the limits of the two RST models are discussed.

5.1.1 Grid Independence Study

As stated by Warren et al.[15], convergence for an adaptive grid relies on a reasonable initial grid on which to complete the adaptation on, otherwise important features may not be flagged for refinement. All features must be adequately modeled so that converged smooth solutions are obtained on the initial grid and do not impact the adaptive meshing process. Therefore, it was deemed important to establish convergence of conditions before and after the shocks on the initial grid.

Three points were selected, one underneath the oblique shock from the tip (200, 24) cm, one in the expected separation zone over the cone but before the flare (240, 28) cm, and one over the flare past all the shock interactions (255, 40) cm. These points were chosen so that they are sufficiently far from the regions where the adaptive meshing is expected to take place (shocks) but also near all the dominant flow features. The adaptive mesh would be used to resolve fine features near the shock, such as the SBLI itself. Three initial grids of varying size were generated by halving the base size in the automated mesher (Fig. 5-1 through 5-3). Pressure and temperature were used as the error indicators as both properties are related to the surface pressure and heat flux on the surface of the flared-cone. Adequate convergence of temperature and pressure translates to convergence in the variables being studied and thus are the only properties recorded for the grid convergence study.

Grid convergence was established once the asymptotic range of convergence was approximately equal to one. In addition, a Richardson extrapolation was performed to determine the results, accounting for error due to discretization (Fig. 5-8). Refinement in the adaptive grid

was achieved with the technique described in Chapter 4. The parameters recorded once grid

convergence was achieved were the surface pressure and heat flux. Important grid convergence

parameters include a pressure gradient refinement threshold of 0.06 and coarsening threshold of

3×10^{-5}. The refinement threshold is based on the smallest cells in the prism layer and the

coarsening threshold based on recommendations by Cross and West[8]. The aspect ratio limit to

stop excessive prism layer refinement was set to 0.5 based on recommendations from Cross and
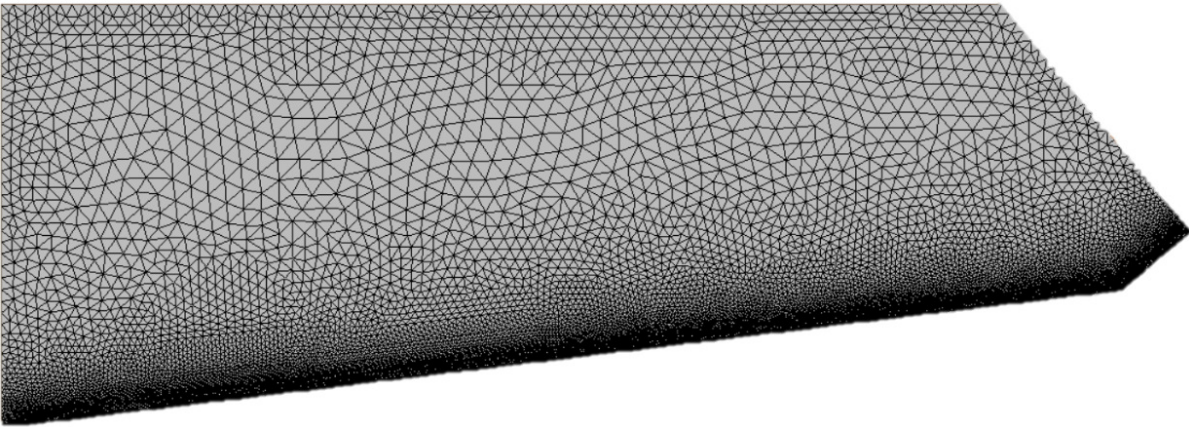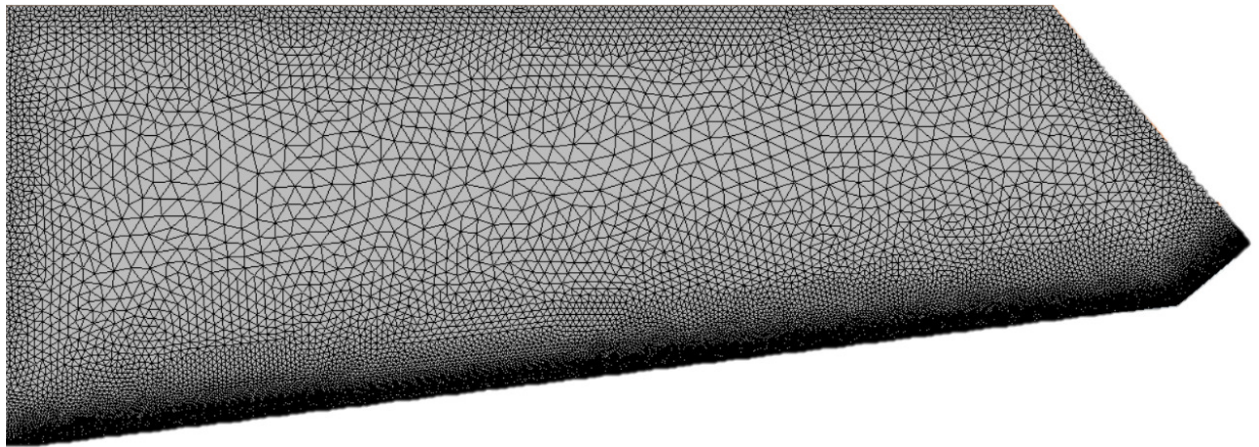
West[8].

Figure 5-1. Coarse initial grid.

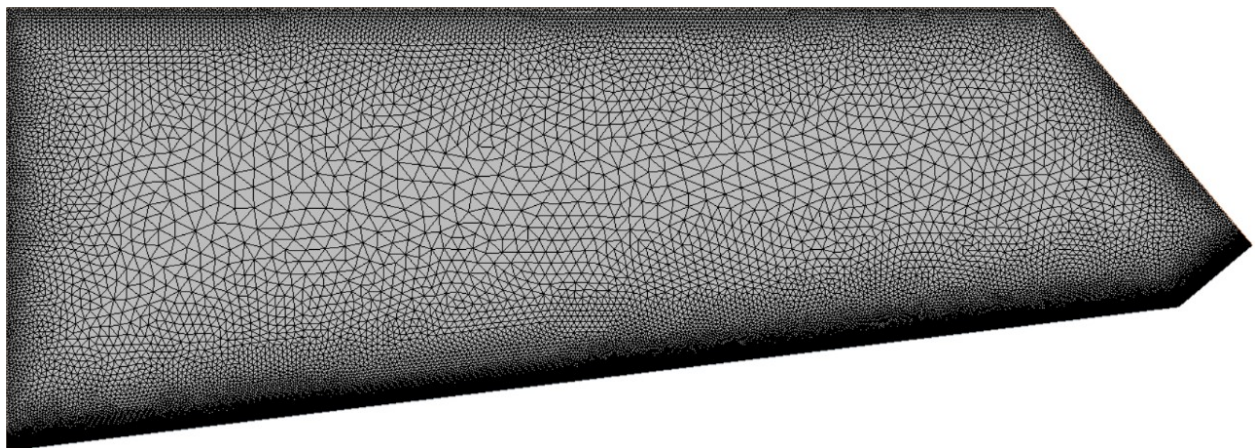Figure 5-2. Medium initial grid.
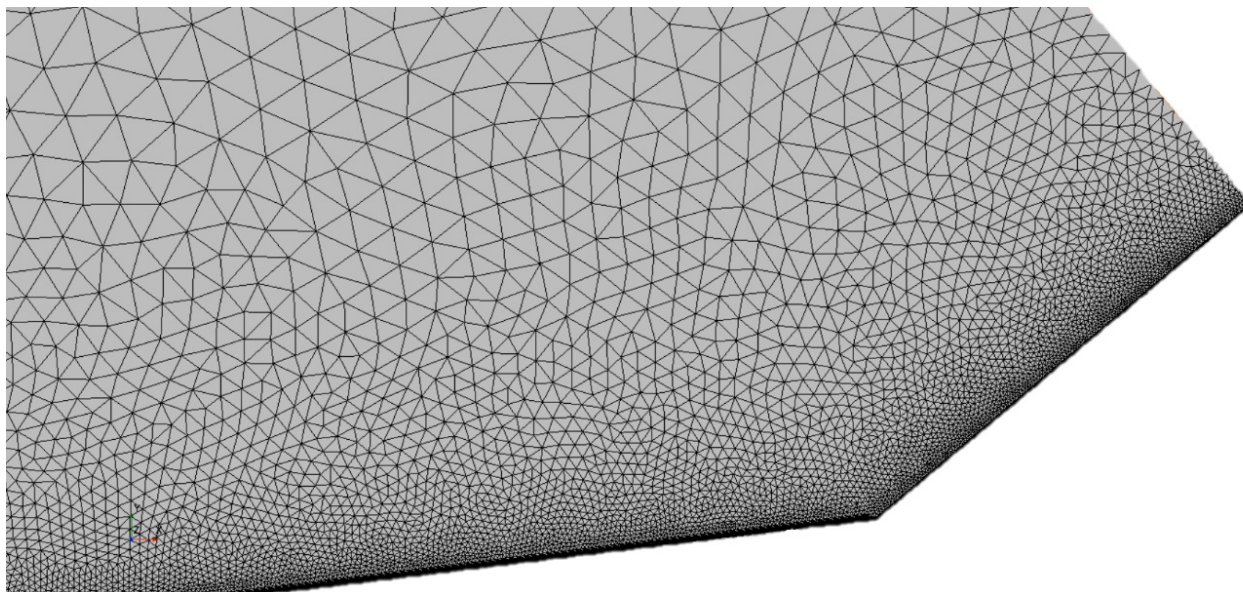

Figure 5-3. Fine initial grid.

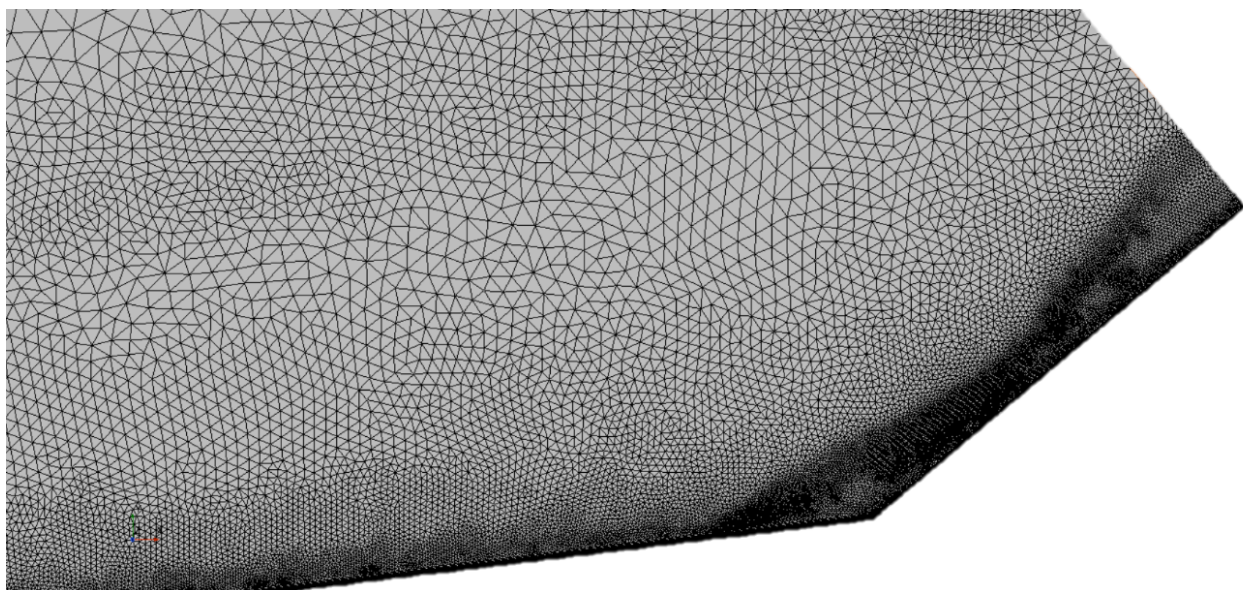Figure 5-4. Close-up of initial grid.

]

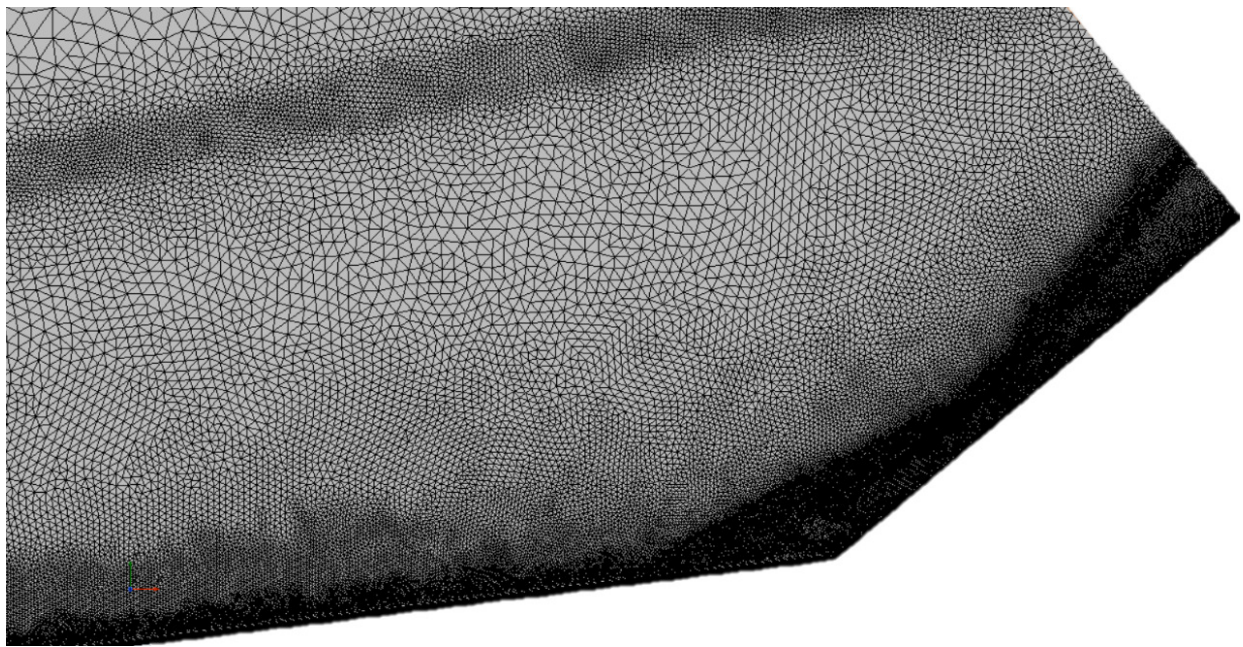Figure 5-5. Close-up of the first adaptive refinement.

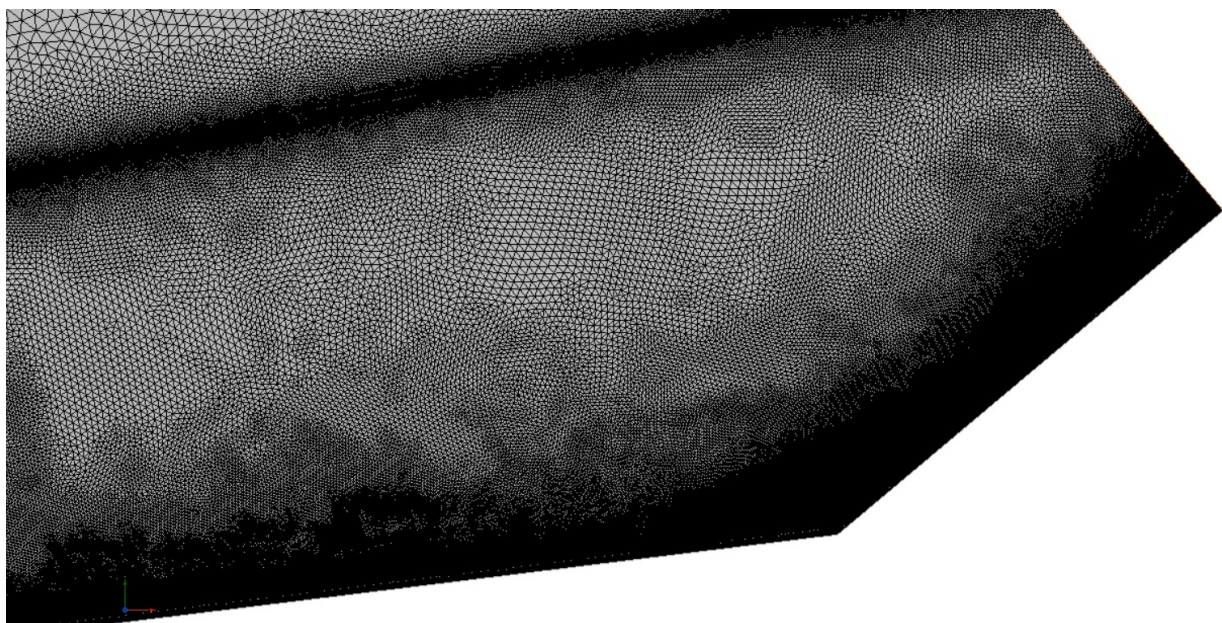Figure 5-6. Close-up of the second adaptive refinement.

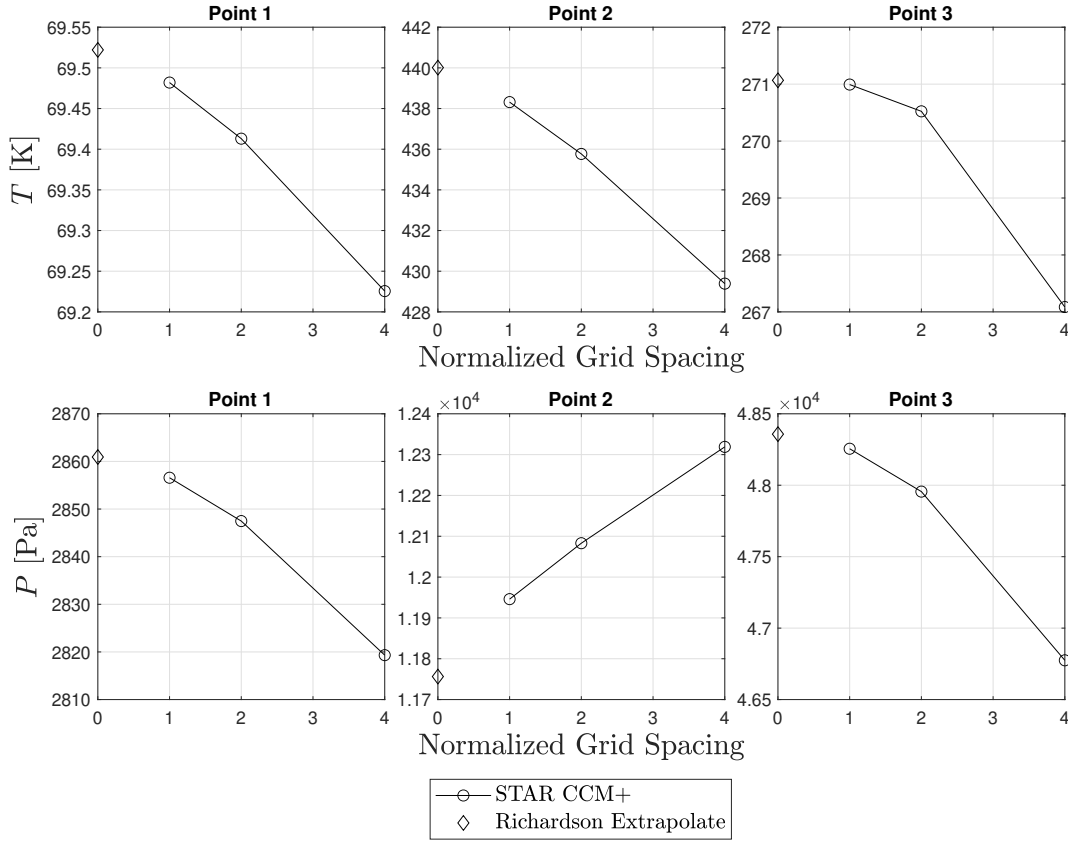Figure 5-7. Close-up of the final adaptive refinement.

Figure 5-8. Fine, medium, and coarse peak value results with Richardson extrapolate.

5.1.2   Shock Wave-Boundary-Layer Interaction Structure

Although a schlieren image of the interaction is provided by Holden et al.[7], no quantitative information was found in regards to the physical location of the interaction, such as the location of the separation shock. Therefore, the prediction of the three turbulence closures that is most similar to the experimental schlieren is selected as a benchmark for quantitive physical comparison of the shock structure. The k-ω SST model correlated well with the experimental schlieren image[7], although a slight increase in separation length was noted along with an earlier separation point, see Fig. 5-9. The k-ω SST predictions is selected as the benchmark to compare with the RST model predictions. This model predicted a separation length of 12 cm and an initial SBLI location at $x = 232$ cm from the inlet boundary. The RST LPS model had the least accurate prediction of the flow structure, with a nearly muted response to the adverse pressure gradient at the initial SBLI, see Fig. 5-10. This consequentially resulted in poor prediction of the separation

length (18.5 cm) and initial SBLI location ($x = 226$ cm). In addition, multiple flow separation eddies formed in the solution and caused multiple oblique shocks and expansions to form (Fig. 5-13). This radically changed the shock-shock interaction and thus impacted the downstream solutions significantly by creating multiple shock-shock interactions and slip lines. The RST elliptic blending closure predicted the separation shock location at $x = 218$ cm and the separation length as 36 cm, 3 times the length of the k-ω SST model predictions. This also led to an incorrect re-attachment point far downstream, which resulted in incorrect heat flux predictions both location and magnitude wise. Since the initial SBLI was shifted forward, the shock-shock interaction was moved far downstream where the post SBLI region would be located outside the computational domain, see Fig. 5-11. Although the separation shock location was too far forward, the RST elliptic blending closure did predict the correct flow structure, with one large eddy (Fig. 5-14) in the separation zone as seen in the experiment. A single λ shock was observed along with part of the resulting slip line.
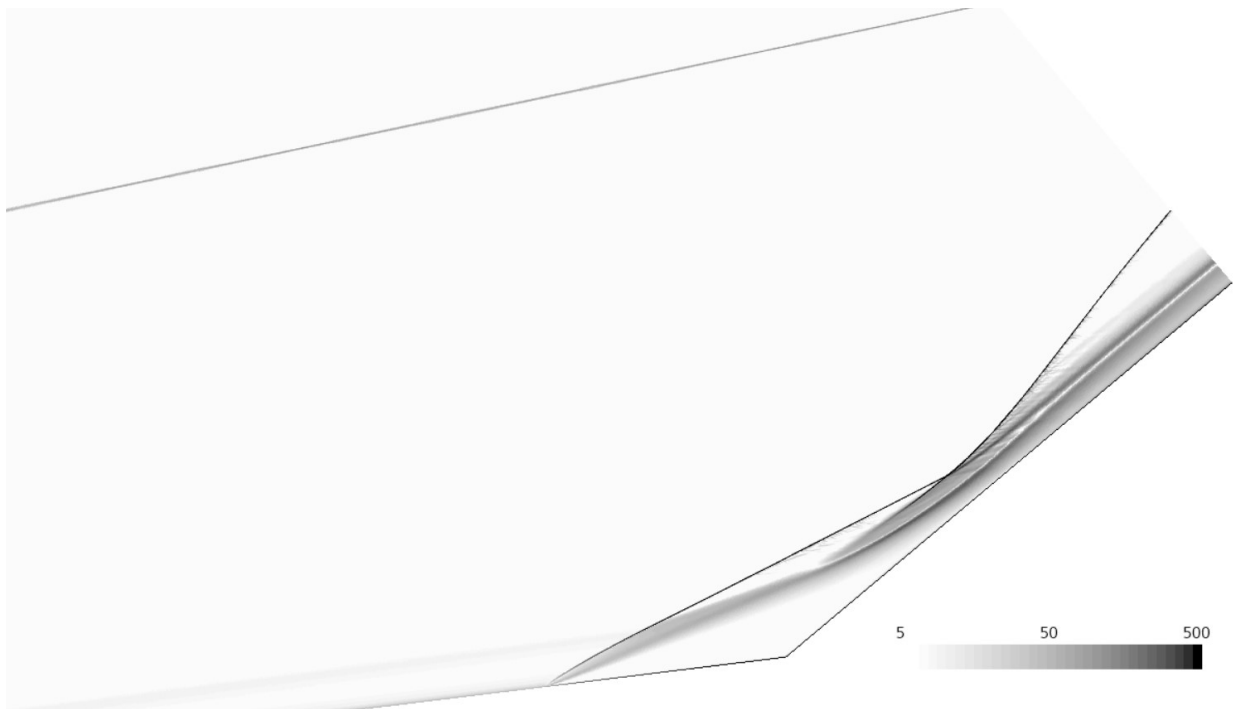

Figure 5-9. Numerical Schlieren of the SST predictions with color bar representing density gradient $\nabla \rho$.

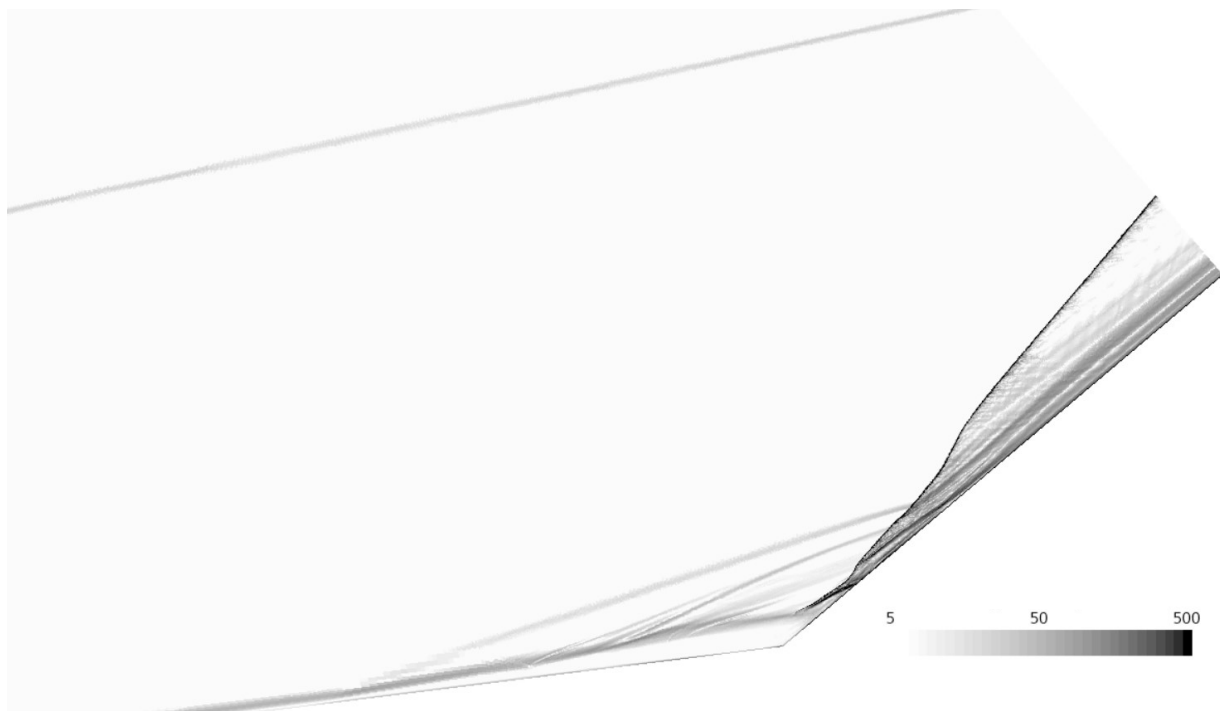Figure 5-10. Numerical Schlieren of the RST LPS predictions with color bar representing density gradient $\nabla \rho$.
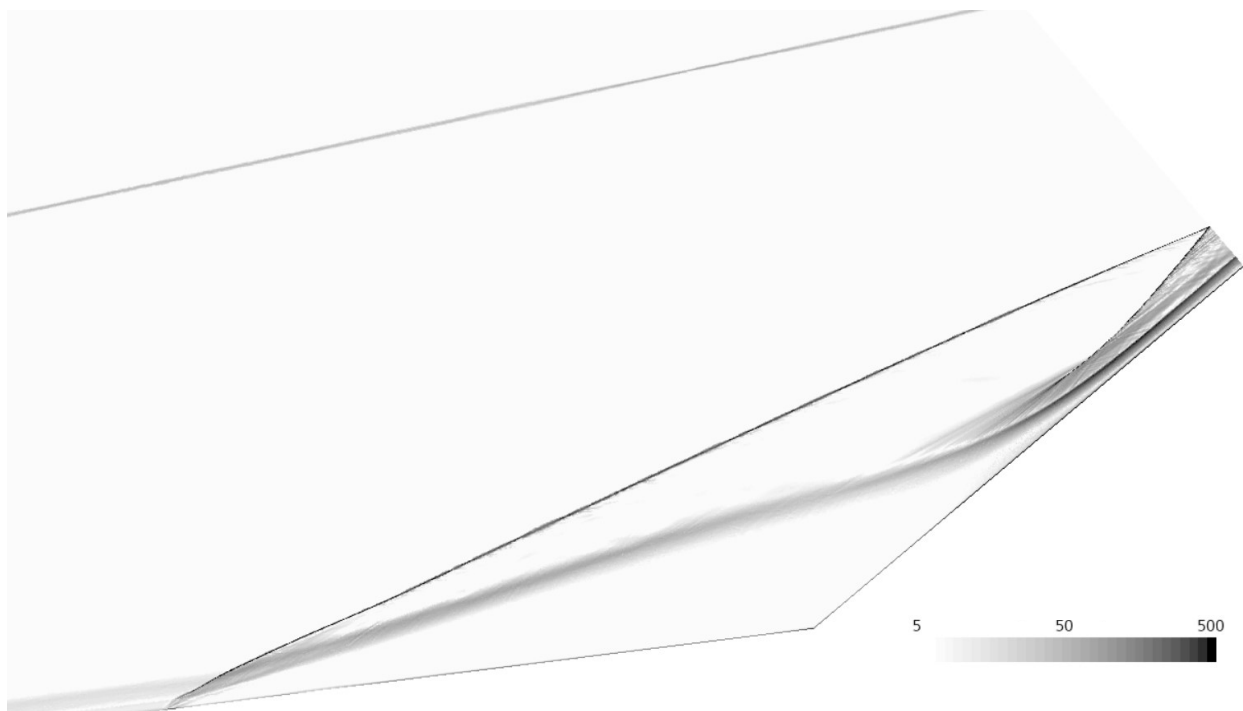

Figure 5-11. Numerical Schlieren of the RST elliptic blending predictions with color bar representing density gradient $\nabla \rho$.
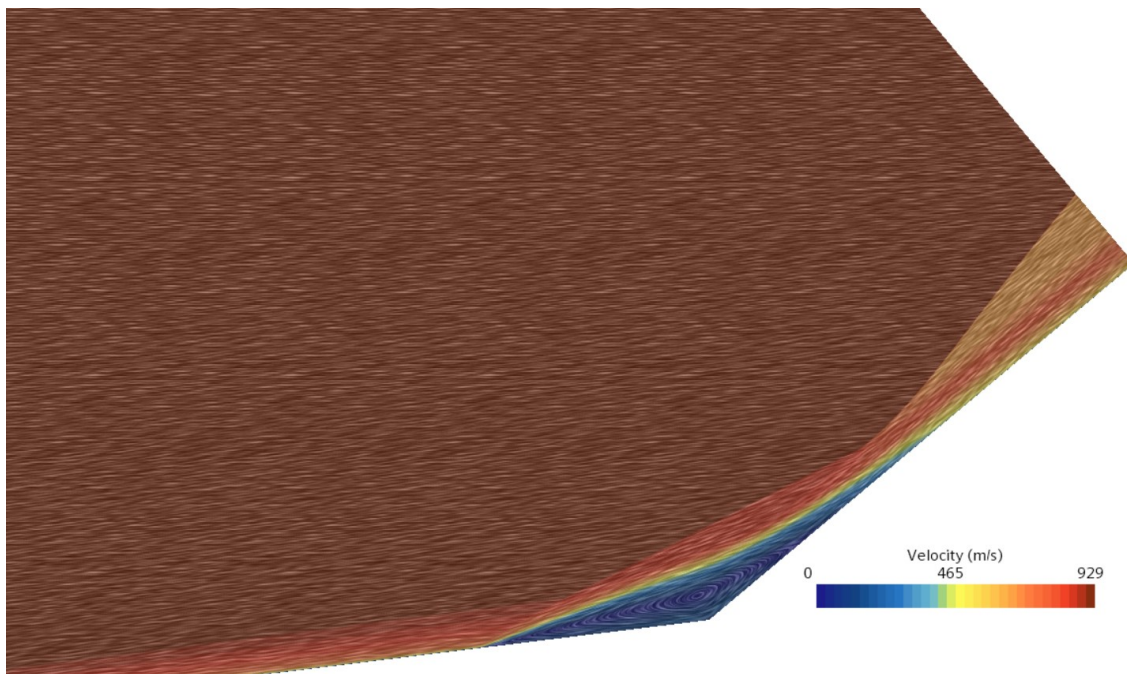
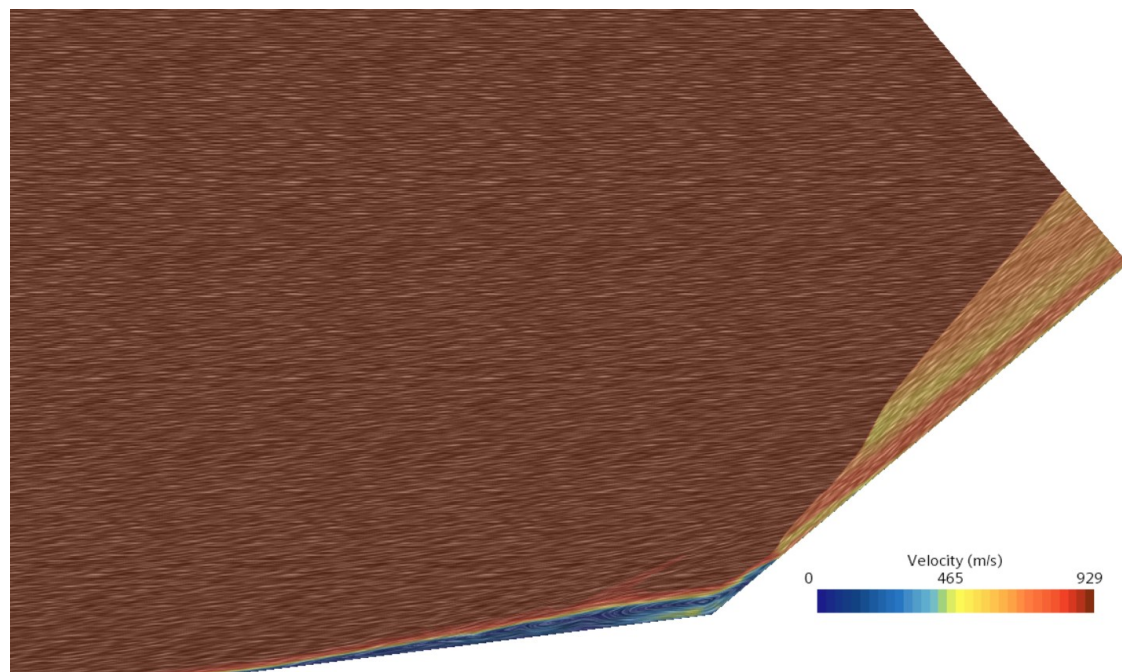Figure 5-12. Line integral convolution of velocity for the SST predictions.

Figure 5-13. Line integral convolution of velocity for the RST LPS predictions.
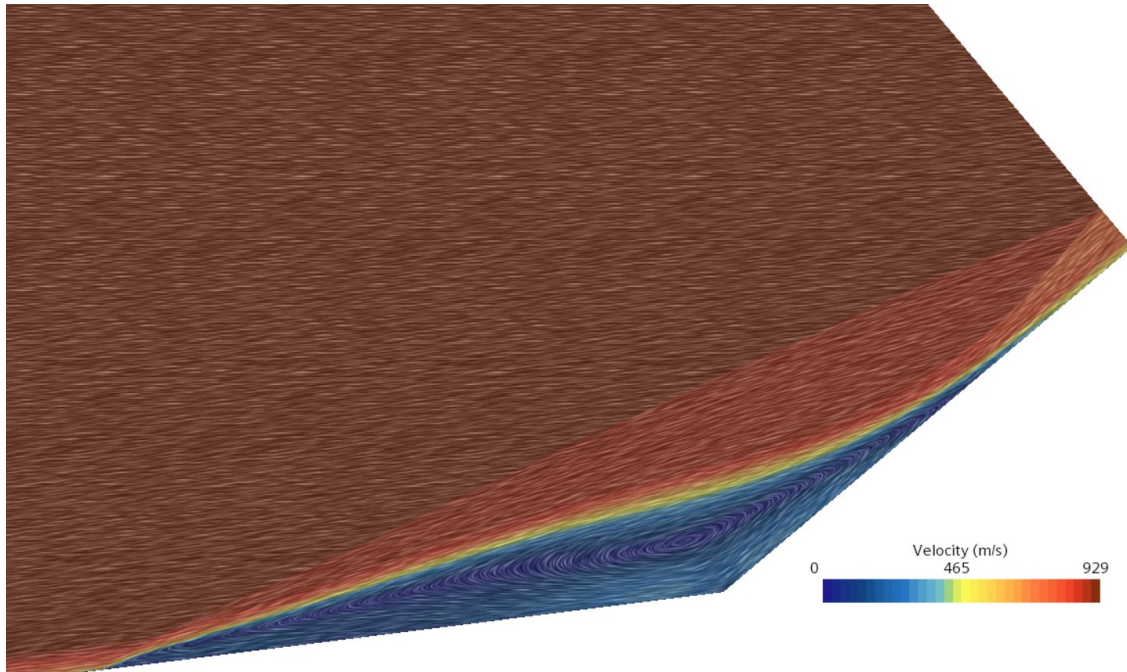
Figure 5-14. Line integral convolution of velocity for the RST elliptic blending predictions.

5.1.3 Boundary Layer Results

Two locations were checked for boundary layer profiles: at a point on the cone, 185 cm from the tip, and on the flare, 245 cm from the tip. The first point was used to check CFD results against theory in a fully turbulent boundary layer. The point was located 30 cm in front of the furthest separation point in all three cases with the aim to be sufficiently far from the transition point. The second point was to check the boundary layer prediction past the SBLI and near the slip line. This point was located far enough along the flare so that it was past all interactions in all three turbulence model simulations. For the law of the wall, the von kármán constant used was 0.41 and the coefficient C+ was 5.5. Results are shown in Fig. 5-15. At the $x = 185$ cm, both the k-ω SST and RST elliptic blending results predict reasonable boundary layer profiles, indicating proper prism layer refinement. The RST LPS model exhibits a fully laminar boundary-layer at this location This shows that the RST LPS closure does not model transition well enough to predict its correct location. In fact, the boundary layer remains laminar until the first SBLI. Only after this disturbance, does the profile change (flow separates). Further results with the RST LPS model are not expected to correlate well with the two other models and the experimental data as

we are focusing on a turbulent shock wave-boundary-layer interaction, thus the phenomena occurring based on the RST LPS closure is not of interest to this work. Near the shear layer, both the eddy-viscosity and RST LPS models perform well and follow the composite law of the wall profile with a max error of 10% for the RST LPS predictions and 4% for the eddy-viscosity closure. The elliptic blending model exhibits a decrease in $U+$ in the log layer, resulting in a maximum error of 25%. The cause for this is unclear.
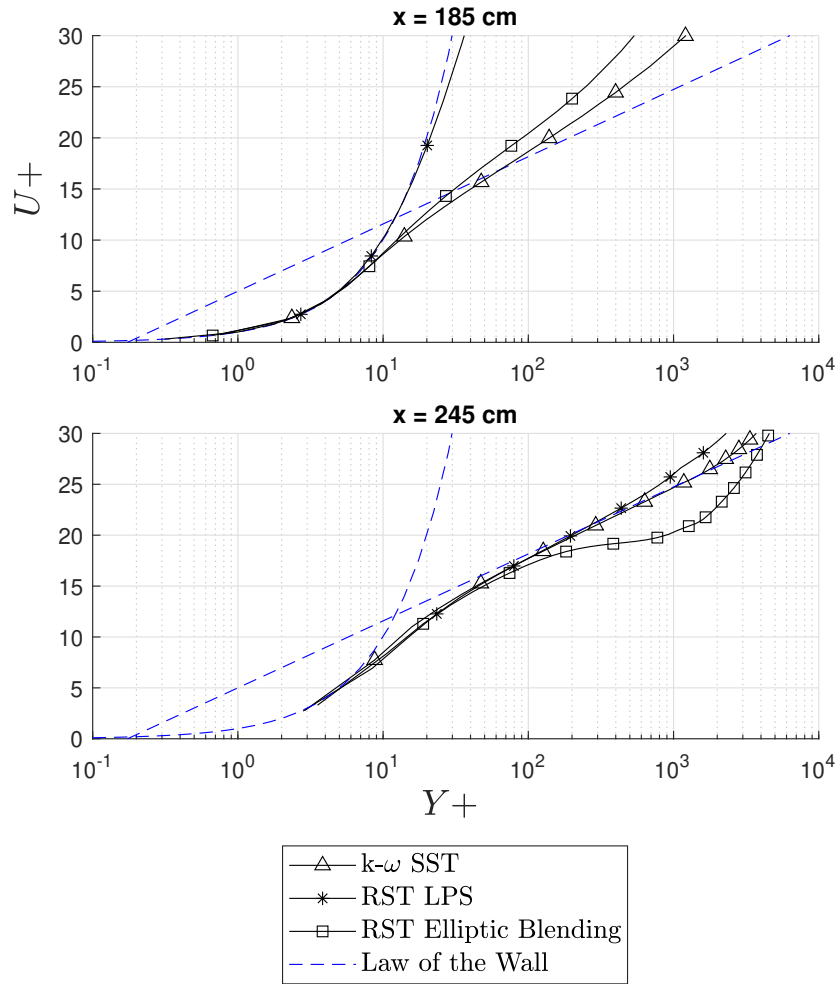

Figure 5-15. Boundary layer profiles at various locations on the body.

5.1.4 Surface Pressure Results

Surface pressure results depend highly on the SBLI structure. Therefore, it is expected that both RST models will have less-accurate results compared to the k-ω SST closure. This is

apparent in Fig. 5-16. The RST elliptic blending model over-predicts the peak surface pressure by 37% while the RST LPS over-predicts by 51%. The magnitude and location error of the surface pressures for the RST models is attributed to poor separation modeling. The presented predictions with the k-ω SST model tend to align with experimental data more closely than both RST predictions and the results of Cross and West[8] with the same two-equation model. The k-ω SST model predictions have the peak heat flux 1.5 cm behind the experimental peak while the RST LPS and elliptic blending predictions is 3 cm forward and 7 cm behind, respectively. This model is the most accurate of the three in regards to the peak surface pressure location as well as the initial jump at the $x = 232$ cm in the surface pressure where the SBLI begins.

Figure 5-16. Surface pressure along the SBLI region as predicted by RST and eddy-viscosity models. Experimental data from Holden et al.[7] and results from Cross and West[8] shown for comparison.

5.1.5 Heat Flux Results

Heat flux predictions showed a similar trend to the surface pressure predictions: the eddy-viscosity model out-performed the RST models in terms of peak magnitude location, see Fig. 5-17. The k-ω SST peak prediction was 1.5 cm behind the experimental peak while the RST

LPS was 2.5 cm in front and the elliptic blending was 7.5 cm behind. The RST elliptic blending over-predicts peak heat flux by 37% while the RST LPS over-predicts by 198%. The k-ω SST model over-predicted by 85%. As evidenced, all the RANS models tested in this work tend to over-predict the peak heat flux. This is because turbulence models typically focus on predicting accurate momentum transfer as opposed to heat transfer. Turbulent momentum and heat transfer are fundamentally different processes. The largest eddies determine the Reynolds stresses while heat transfer occurs on a much smaller scale and is less directly related to the large eddies[1].
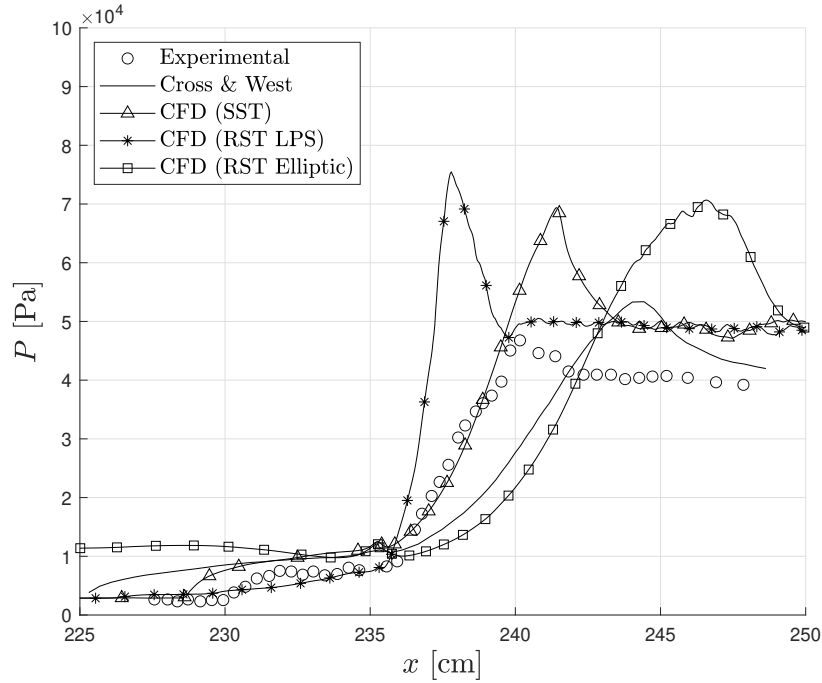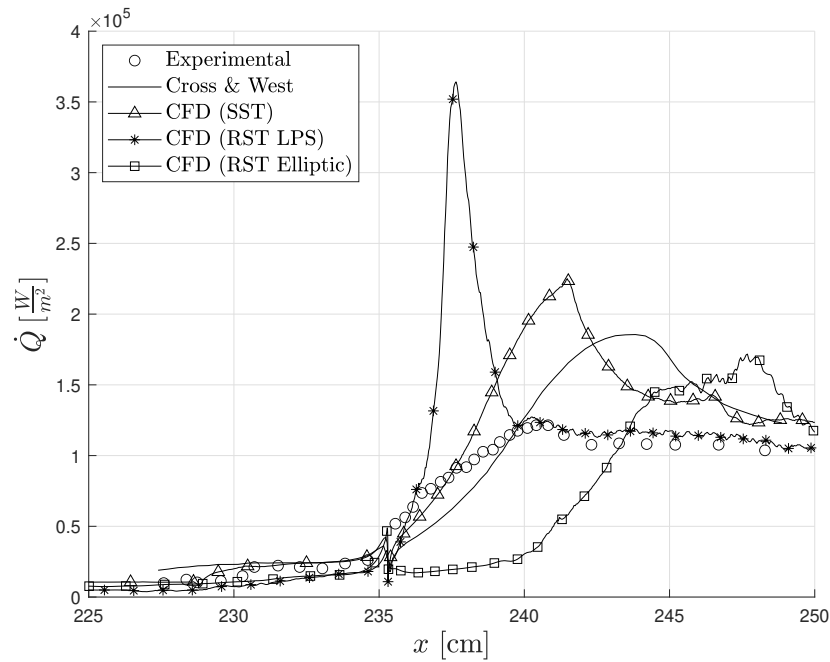

Figure 5-17. Heat flux along the SBLI region as predicted by RST and eddy-viscosity models. Experimental data from Holden et al.[7] and results from Cross and West[8] shown for comparison.

5.1.6 Discrepancy Between Published Results

Efforts were made to replicate the results of Cross and West[8] using the same solver settings and turbulence model (k-ω SST) to double check correct model selection and grid quality. It is noted that the location of the peak values predicted by Cross and West[8] are further aft, predicting the peak for surface pressure 4 cm behind the experimental data and 3.5 cm behind for the peak heat flux. The results from this study with the same model only predicted the peak 1.5 cm behind

the experimental data for both pressure and heat flux. Additionally, the initial jump at the separation shock in both results is missing entirely. This was replicated by allowing the results to converge fully on an initial grid that was too coarse before the next refinement was performed in the set of adaptive mesh refinements. Allowing full convergence on a coarse grid tended to dissipate results and thus did not capture the large gradients that led to jumps in the surface variables. The grid convergence study also displayed that the peak surface pressure and heat flux location prediction moved rearward as the grid became coarser. Therefore, it is believed that full convergence was reached between refinement steps and dissipated the results of Cross and West[8]. This explains the smoothing of the initial jump and rearward max pressure and heat flux location.

5.1.7   Separation in Reynolds Stress Transport Closures

The predictions of the RST closures are quite different from the k-ω SST predictions. The most significant difference is the location of the separation on the cone portion of the flared-cone geometry, see Fig. 5-9 through 5-11. One the contributing factors to the poor separation prediction with the RST models is the use of a k-ε closure for the turbulent dissipation rate. The k-ε model is known for poor performance in adverse pressure gradients, which is the cause of the flow separation[1]. The underlying issue is the k-ε model fails to respond in a physically realistic manner to the adverse pressure gradient on the rear-end surface, where the skin friction prediction is too high. This means the vorticity at the surface is too large and diffuses from the surface. This vorticity is swept into the main flow and too strong a vortex forms when the flow separates. This, in turn, reduces the base pressure and distorts the entire flow-field[1]. The results in Fig. 5-18 show that this indeed happens with both RST models. The results in Fig. 5-18 are the skin friction coefficients at the base of the separation shock for all three models. Note that the longitudinal position of the separation shock is different for each model, thus Fig. 5-18 only shows a 2 cm range near the base of each of the respective separation shock locations. No large increase in skin friction coefficient is predicted with k-ω SST model; rather an initial drop by 100 units in skin friction is experienced with a rise to a steady value 63 units smaller than pre-SBLI. The results of the RST elliptic blending model show a similar trend except that the skin friction coefficient

spikes immediately after the large adverse pressure gradient of the SBLI to skin friction coefficent 43 units larger than pre-SBLI. The RST LPS model also predicts an increase in skin friction coefficient by 27 units, rearward of the SBLI, but the response is small compared to that of the two other models. No initial drop in skin friction is experienced like the two other models. This is because the LPS model predictions never transitioned to a fully turbulent boundary layer until after the separation shock, so the increase is due to the boundary changing from laminar to turbulent.
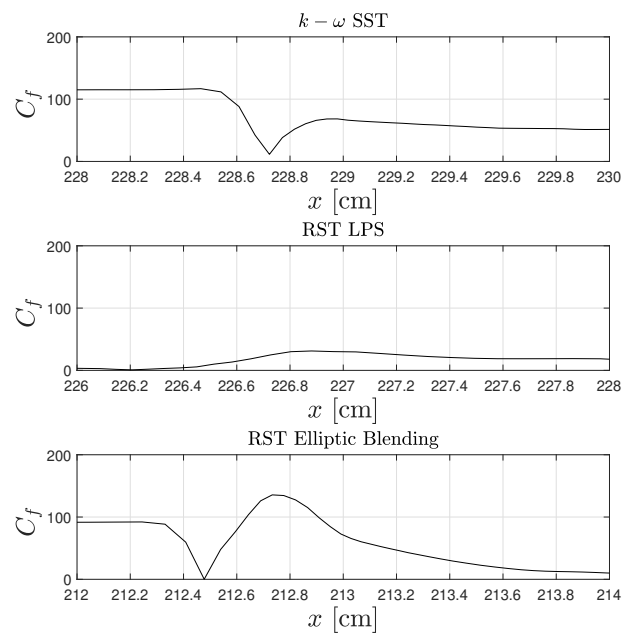

Figure 5-18. Skin friction coefficient at the initial SBLI for the three turbulence model results.

CHAPTER 6
CONCLUSIONS

6.1 Future Work

The turbulence closures used in this work relied on the Morkovin Hypothesis[16]. The hypothesis is the notion that at moderate Mach numbers, the essential dynamics of shear flows follow the same patterns as incompressible flows. This means that dilatation is small and any differences from incompressible turbulence can be accounted for by mean variations of fluid properties. This allows the Navier-Stokes equations to be written in Favré-averaged form and a variable density extension of incompressible turbulence models to compressible flows. Recent studies have shown that the Morkovin hypothesis is valid for the mean field between a freestream Mach number range of 2.24 to 10 with various wall boundary conditions[17−18]. The assumption was also verified for the turbulence field on flat-plate flows[19]. These studies, however, did not have the strong gradients associated with SBLI. Morkovin's hypothesis has further implications that impact the results in this study, namely that of the Strong Reynolds Analogy (SRA). The SRA assumes dynamic similarity between momentum transfer and heat transfer, where the same models for modeling the momentum transport is used for turbulent heat transport[17]. This in turn allows a constant Prandtl number to be used for the closures schemes. SRA pivots on the assumption that pressure and stagnation temperature fluctuations in the boundary layer are small[16]. However, this assumption has been shown to be incorrect for high-speed flows, where variable-Prandtl number turbulence models have shown improved heat flux, surface pressure, and skin friction predictions[20−21]. Mahesh et al.[22] shows the relationship between u' and T' derived from the Morkovin hypothesis, assuming temperature fluctuations are small in the linear limit,

$$\frac{T'}{\overline{T}} = -(\gamma-1)M^2\frac{u'}{U}.$$
(6-1)

By using the Rankine-Hugoniout equations, it is shown that the above relationship cannot be valid if it is assumed to hold upstream of the shock[22]. Additionally, the linearized energy equation,

$$T`_2 + \frac{U_2u'_2}{C_p} = -\frac{\xi_t}{C_p}(U_1 - U_2),$$
(6-2)

can be used to show that, based on the assumption of no temperature fluctuations in front of the shock, that there must be temperature fluctuations past the shock, thus again, invalidating the Morkovin hypothesis. A similar argument is used to explain why the hypothesis does not hold in the far-field. DNS data showed that immediately behind the shock wave, significant levels of stagnation temperature fluctuations are generated due to oscillation of the shock front. The downstream convection of vorticity entropy fluctuations were found to be the cause of the stagnation temperature fluctuations in the far-field of the shock wave. This leads to inapplicability of Morkovin's hypothesis in the far-field because, again, stagnation temperature fluctuations are not negligible[22]. Future work will address this problem of non-negligible temperature fluctations by implementing a variable-Prandtl number formulation into the turbulence closure.

6.2   Concluding Remarks

Simulations of a Mach 6 turbulent SBLI on a flared-come geometry was carried out using an eddy-viscosity model (Menter k-ω SST), and two RST models (linear pressure-strain and elliptic blending). Grid convergence was investigated to ensure the initial grid captured smooth solutions and allowed the adaptive meshing algorithm to refine where needed (near the SBLI). The grid was refined using the normalized pressure gradient technique and was found to sufficently refine the shocks without excessively refining the prism layers.

It was hypothesized that RST models would predict the surface pressure and heat flux in the SBLI region better than the eddy-viscosity model because of the relaxation of the Bousinessq hypothesis, explicitly modeling of all of the Reynold stresses. However, this proved to be incorrect. The eddy-viscosity model correlated the best with the experimental data in terms of location of the peak values and separation. The RST LPS model predicted the peak surface pressure and heat flux forward of the expected location while the RST elliptic blending predicted the maximum values too far rearward. Both RST models over-predicted the separation length, with the elliptic blending over-predicting by 200% and the LPS model by 54%. All models over-predicted the peak heat flux by at least 37% and by at most 198%. Similar over-prediction of the peak wall pressure resulted from all three models, with an over-prediction range of 30%-50%.

Boundary layer statistics show that the RST LPS model was unable to predict transition from a fully laminar to a turbulent boundary layer, and thus resulted in a laminar SBLI. The RST LPS model also incorrectly predicted multiple separation bubbles in the SBLI region and thus multiple oblique shocks formed. The RST elliptic blending and eddy-viscosity model correlated with the expected SBLI structure from the experiment, with a single separation shock on the cone and a λ-shock interaction on the flare. However, due to the k-ε model used for the turbulent dissipation in the RST models, the response to the adverse pressure gradient was incorrect and increased the skin friction too much directly behind the initial separation shock and thus led to a large separation bubble. This is a common problem with the k-ε model that has been well documented over the decades[1]. Possible explanations for the over-prediction of the heat flux are the use of the Morkovin hypothesis in a high-speed flow with a large pressure gradient in the boundary-layer. Similarly, the Reynolds analogy that allows a constant Prandtl number to be specified can fall short, where different mechanisms exist for momentum and turbulent heat transport.

REFERENCE

[1] Wilcox, D. C., *Turbulence Modeling for CFD*, DCW Industries, La Canada, CA, 1993.

[2] Babinsky, H., and Harvey, J. K., *Shock Wave-Boundary-Layer Interactions*, Cambridge University Press, New York, USA, 2014.

[3] Spalart, P. R., "Strategies for Turbulence Modelling and Simulations," *International Journal of Heat and Fluid Flow*, Vol. 21, No. 3, 2000, pp. 252–263.

[4] Cécora, R.-D., Eisfeld, B., Probst, A., Crippa, S., and Radespiel, R., "Differential Reynolds Stress Modeling for Aeronautics," *50th AIAA Aerospace Sciences Meeting including the New Horizons Forum and Aerospace Exposition*, Nashville, Tennessee, 2012.

[5] Launder, B. E., and Shima, N., "Second-Moment Closure for the Near-Wall Sublayer: Development and Application," *AIAA Journal*, Vol. 27, No. 10, pp. 1319-1325, 1989.

[6] Lardeau, S., Manceau, R., "Computations of complex flow configurations using a modified elliptic-blending Reynolds-Stress model," *10th International ERCOFTAC Symposium on Engineering Turbulence Modelling and Measurements*, Marbella, Spain, 2014.

[7] M. S. Holden, T. P. Wadhams, and M. MacLean. "Measurements in Regions of Shock Wave/Turbulent Boundary Layer Interaction From Mach 4 to 10 for Open and 'Blind' Code Evaluation/Validation," *21st AIAA Computational Fluid Dynamics Conference*, San Diego, California, June 2013.

[8] Cross, P. G., and West, M. R., "Simulation of Hypersonic Flowfields Using STAR-CCM+," Naval Air Warfare Center Weapons Division, TM 8824, 2018.

[9] Menter, F. R., "Two-Equation Eddy-Viscosity Turbulence Models for Engineering Applications," *AIAA Journal*, Vol. 32 No. 8, pp. 1598-1605, 1994.

[10] Gupta, R. N., Lee, K. P., Thompson, R. A., and Yos, J. M., "Calculations and Curve Fits of Thermodynamic and Transport Properties for Equilibrium Air to 30000 K," NASA STI/Recon Technical Report N, 92, 11285, 1991.

[11] Lien, F. S., and Leschziner, M. A., "Assesment of Turbulence-Transport Models Including Non-Linear RNG Eddy-Viscosity Formulation and Second-Moment Closure for Flow Over a Backward-Facing Step," *Computers Fluids*, Vol. 23 No. 8, pp. 983-1004, 1994.

[12] Sarkar, S., and Balakrishnan, L., "Application of a Reynolds-stress Turbulence Model to the Compressible Shear Layer," *AIAA Journal*, Vol. 29 No. 5, pp. 743-749, 1990.

[13] Gibson, M. M., and Launder, B. E., "Ground effects on pressure fluctuations in the atmospheric boundary layer," *Journal of Fluid Mechanics*, Vol. 86 Pt. 3, pp. 491-511, 1990.

[14] Speziale, C. G., Sarkar, S. Gatski, T. B., "Modelling the pressure-strain correlation of turbulence: an invariant dynamical systems approach," *Journal of Fluid Mechanics*, Vol. 227, pp. 245-272, 1991.

[15] Warren, G. P., Anderson, K., Thomas, J. L.,and Krist, S. L., "Grid Convergence for Adaptive Methods," *10th Computational Fluid Dynamics Conference*, Honolulu, Hawaii, 1991.

[16] Morkovin, M., "Effects of Compressibility on Turbulent Flows," Mecanique de le Turbulence, edited by A. Favre, Gordon and Breach, New York, 1964, pp. 367–380.

[17] Sommer, T. P., So, R. M. C., and Zhang, H. A., "Near-Wall Variable Prandtl-Number Turbulence Model for Compressible Flows," AIAA Journal, Vol. 31, No. 1, 1993, pp. 27–35.

[18] Huang, P. G., Bradshaw, P ., and Coakley, T. J., " A Skin Friction and Velocity Profile Family for Compressible Turbulent Boundary Layers," AIAA Journal, Vol.31, 1993, pp.1600–1604.

[19] So R. M. C., Gatski, T. B., and Sommer, T. P., " Morkovin Hypothesis and the Modeling of Wall-Bounded Compressible Turbulent Flows," AIAA Journal, Vol.36, No. 9, 1998, pp.1583–1592.

[20] Xiao, X., Edwards, J. R., Hassan, A. H., and Gaffney, R. L.,"Role of Turbulent Prandtl Numbers on Heat Flux at Hypersonic Mach Numbers," AIAA Journal, Vol. 45, No. 4, 2007, pp. 806–813.

[21] Roy, S., Pathak, U., and Sinha, K., "Variable Turbulent Prandtl Number Model for Shock/Boundary-Layer Interaction", AIAA Journal, Vol.56, No.1, 2018, pp. 342-355.

[22] Mahesh, K., Lele, S., Moin, P., "The influence of entropy fluctuations on the interaction of turbulence with a shock wave," Journal of Fluid Mechanics, Vol. 334, 1997, pp. 353-379.